Conduction and Electric Field Effect in Ultra-Thin Tungsten Films

Kees van der Zouw , Antonius A. I. Aarnink, Jurriaan Schmitz , and Alexey Y. Kovalgin

Abstract—Ultra-thin tungsten films were prepared using hotwire assisted atomic layer deposition. The film thickness ranged from 2.5 to 10 nm, as determined by spectroscopic ellipsometry and verified by scanning electron microscopy. The films were implemented in conventional Van der Pauw and circular transmission line method (CTLM) test structures, to explore the effect of film thickness on the sheet and contact resistance, temperature coefficient of resistance (TCR), and external electric field applied. All films exhibited linear current-voltage characteristics. The sheet resistance was shown to considerably vary across the wafer, due to the film thickness non-uniformity. The TCR values changed from positive to negative with decreasing the film thickness. A field-induced modulation of the sheet resistance up to $\sim 4.6 \cdot 10^{-4}$ V^{-1} was obtained for a 2.5 nm thick film, larger than that generally observed for metals.

Index Terms—Thin films, tungsten, hot-wire, atomic layer deposition, spectroscopic ellipsometry, scanning electron microscopy, X-ray diffraction, sheet resistance, contact resistance, transfer length, temperature coefficient of resistance, field effect.

I. INTRODUCTION

THE CONTINUOUS downscaling of electronic devices poses an increasing demand for the use of ultra-thin films in a variety of applications such as microprocessors, image sensors, memories, and physical unclonable-function devices [1], [2]. Both isolating and metallic layers are widely requested. Among a variety of characteristics, film conformality, uniformity, thickness, step coverage and resistivity may be of crucial importance. Tungsten (W) is one of the metals commonly adopted by industry in integrated circuits to realize electrodes and interconnects [3]. With decreasing the film thickness, the main challenge is to keep the sheet and contact resistances low enough, in line with the application demands [4]. Further, the ultra-thin metal films may be expected to exhibit a field effect, which is not observable in the thick layers due to the high electron density and the related screening effect [5]–[10]. All this makes determining the electrical behavior of ultra-thin W films relevant and important.

Atomic Layer Deposition (ALD) is a deposition technique that perfectly fits with the need for miniaturization. ALD is known to provide high layer uniformity and conformality, together with excellent step-coverage and precise layer-thickness control, due to its attribute of sequential, self-limiting surface reactions [11]. This makes ALD the method of choice for many applications. ALD can be categorized in two main classes: thermal ALD and radical enhanced ALD (REALD). Many single element deposition processes can not be executed in pure thermal mode [11], [12]. Radicals enable reactions which would otherwise not occur. A plasma is often used as a source of radicals. However, there is a number of drawbacks while using a plasma. First, a plasma can damage the wafer. Secondly, multiple reactions take place in plasma: the wafer may be exposed to unwanted radicals, atoms, ions, or UV photons [13]. Recently, a novel approach to ALD was developed, the so-called hot-wire assisted ALD (HWALD) [14]. A hot-wire takes the role of the plasma as the radical source. HWALD has been successfully applied to deposit either α- or β-phase crystalline W, depending on the conditions [15]–[19].

In this work, we applied conventional Van der Pauw and circular transmission line method (CTLM) test structures, to explore the electrical properties of HWALD W films grown in the thickness range of 2.5–10 nm. The influence of film thickness on the sheet and contact resistance, temperature coefficient of resistance (TCR) and external electric field effect (FE) were studied. This work extends our previous ICMTS 2019 publication [20] by adding a detailed analysis of the W-film thickness with spectroscopic ellipsometry (SE), further verified by high resolution scanning electron microscopy (SEM). X-ray diffraction (XRD) analysis of the crystal structures of HWALD W films is additionally provided.

II. TEST STRUCTURE FABRICATION

Highly doped p-type 4-inch (100) Si wafers were used as substrates (see Fig. 1 for the process flow). Prior to thermal oxidation, the wafers were ozone-steam cleaned, followed by an 1% HF deep for 1 min. Oxidation was carried out at 1100 °C for 45 minutes in dry oxygen, to obtain approximately 100 nm of SiO_2. Photoresist was applied and patterned according to the desired electrode shapes. Sputtering of a 10-nm-thick titanium adhesion layer and 40 nm thick platinum (Pt) layer was followed by a lift-off step to pattern the Pt electrodes. In our fabrication process, the electrodes are deposited before the to-be-analyzed W film, mainly to
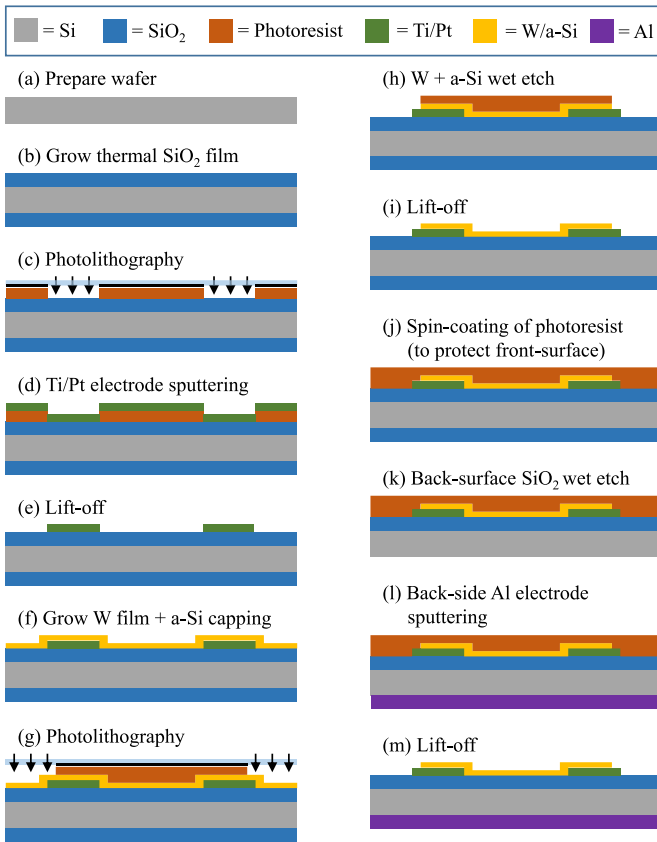
Fig. 1. Schematic of the process flow to fabricate the test structures. The process steps are treated in more detail in Section II.

minimize processing on top of fragile ultra-thin layers. In electrical measurements, probes can easily pierce through the top layers to reach the electrodes. Next, a tungsten film and an a-Si capping layer (to prevent oxidation of the W in air) were deposited by HWALD and chemical vapor deposition (CVD), respectively. Further patterning was performed by a second lithography step, subsequent wet-etching of the W and a-Si layers in a solution containing 0.67% of HF and 50% of HNO_3, and by stripping the photoresist in fuming HNO_3. A new layer of photoresist was applied to protect the front-surface during the back-side SiO_2 removal in buffered HF. Sputtering of a 400-nm-thick aluminum film as the back-side (gate) electrode finalized the structures.

The HWALD deposition of W was performed from tungsten-hexafluoride (WF_6) and hydrogen (H_2) precursors at a substrate temperature of 275 °C. The hot-wire dissociates the H_2 into atomic hydrogen (at-H) radicals. A hot-wall reactor was used to grow low-resistivity α-phase W films [18]. No growth of W was observed on SiO_2 directly [19]. To initiate the HWALD growth of W, a CVD a-Si seed layer is grown on top of the SiO_2 by dissociation of trisilane (Si_3H_8), and subsequently converted into a W seed layer by introducing WF_6 into the reactor.

III. Test Structure Design

Each wafer is subdivided into process evaluation modules (PEMs). The PEM layout is shown in Fig. 2(a). Each PEM
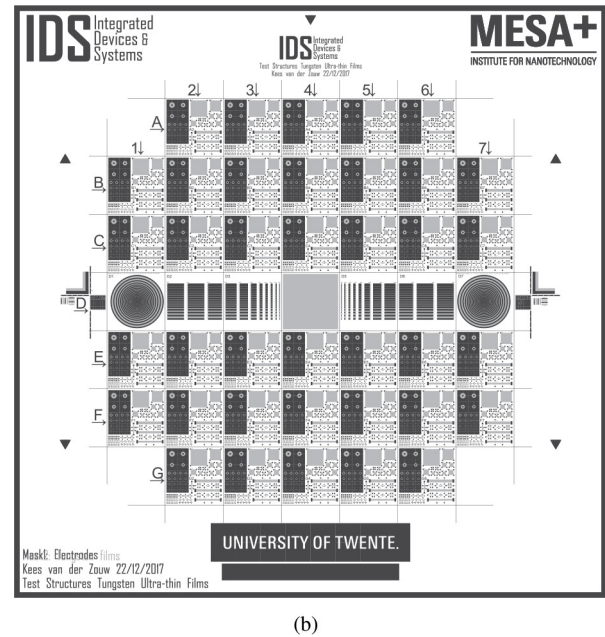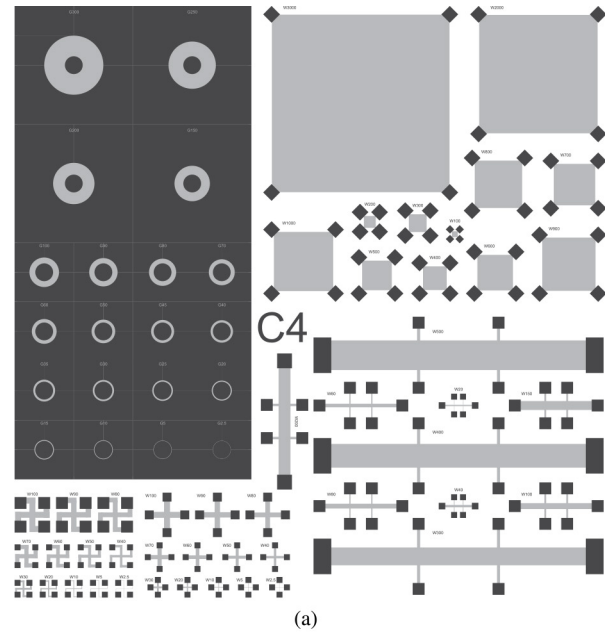

Fig. 2. (a) The process evaluation module with different test structures. (b) The wafer layout including all the modules.

consists of several Van der Pauw, CTLM, Greek-cross and Hall structures of various dimensions. As shown in Fig. 2(b), the PEMs were evenly distributed across the wafer surface.

For each type of structure, several issues were considered in the design process. Only the considerations for the Van der Pauw and CTLM structures will be discussed in detail, since all results presented in this work involve measurements on these structures. The Van der Pauw equation for the sheet resistance holds for the ideal case of infinitesimally small contacts at the circumference of the sample [21], [22]. In practice, this condition is hardly met and a correction factor should be included. The design of the Van der Pauw structures used in this work (see top of Fig. 3) is based on the symmetrical
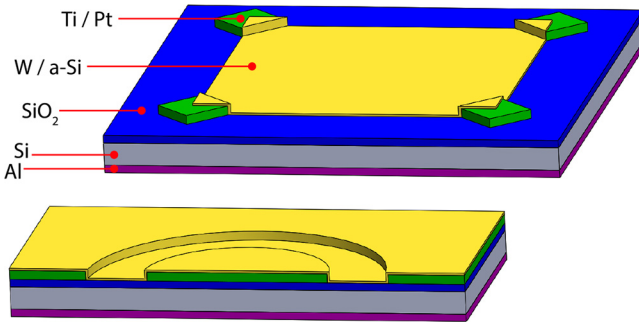
Fig. 3.   Schematic representation of the typical test structures used in this work. (Top) The Van der Pauw structure. (Bottom) the CTLM structure. The dimensions are not to scale.

octagon structure that was analytically treated by [23], it also has electrodes located at the corners of the sheet. The ratio between the contact length and the total length of the structures at the circumference of the structure is kept around 0.1 for each structure, which means that the Van der Pauw equation should hold with high accuracy [23]. Small deviations of the electrode placement can be expected due to the alignment inaccuracy during fabrication. This was kept within 1 μm. Initial dual configuration measurements on the wafer with the 10-nm W film showed that the asymmetry in the measured sheet resistance (R_{sh}) was below 1% and therewith considered negligible. Small adaptations to the design can be applied to decrease sensitivity to alignment accuracy.

The CTLM structures, as designed for this work, have a circular inner electrode, separated from the outer electrode by a gap W_g (variable), as shown at the bottom of Fig. 3. By choosing a radius for the inner electrode (R_{el}) much larger than W_g and four times the transfer length (L_T), the values for R_{sh}, L_T and the contact resistance (R_C) can be extracted from the corresponding resistance versus W_g plot [24], [25]. It is assumed that the electrode resistance is negligible and the W sheet resistance on top of the electrodes and within the gap is identical [26], [27]. The main difficulty in the design process of the CTLM structures is related to finding the L_T. L_T is the length over which the electrical current is transferred between the electrodes and the W sheet. It can be extracted experimentally, however, an educated guess of its magnitude has to be made beforehand to meet the $R_{el} \gg 4L_T$ condition. In this work, the R_{el} was chosen at 150 μm.

IV. OPTICAL MEASUREMENT RESULTS

The thickness of the HWALD W was monitored *in-situ* by spectroscopic ellipsometry (SE). SE is generally used to determine the layer thickness (t) and optical constants (ϵ_1, ϵ_2). SE is a non-destructive optical characterization technique in which the change in polarization of a light beam upon reflection at the sample is monitored. The change in polarization is measured through the experimentally measured psi (Ψ) and delta (Δ) parameters [28], [29]. Especially Δ is a sensitive measure of the thickness of ultra-thin films. For the majority of samples, no simple relation exists between the measured (Ψ,Δ) and desired (ϵ_1,ϵ_2,t) quantities. It is therefore necessary to propose a model that adequately describes ϵ_1, ϵ_2 and t of all

the layers and compare the model against the measurement results. The accuracy of the model is determined by the mean square error (MSE), which mathematically quantifies the difference between the experimental and model-generated data. In this work, the *in-situ* SE monitoring was performed by a Woollam M2000 spectroscopic ellipsometer operating in the wavelength range between 254 and 1688 nm, in combination with COMPLETEEASE modeling software.

In this work, an optical model is proposed comprising of a silicon substrate, a thermally grown SiO_2 layer and the HWALD W layer. The optical properties of Si [30] and SiO_2 [31] are taken from the software database. In earlier research, the dielectric function of tungsten was determined for several wavelength ranges [32], [33]. It was shown that the dielectric function can be parameterized by applying the Drude-Lorentz model. A Drude term describes the intraband absorption, whereas Lorentz oscillators describe the interband absorption by electrons [34], [35]. Importantly, the optical properties of ultra-thin tungsten are unknown and expected to be significantly different from those of the bulk material [36]–[39]. Consequently, the optical properties have to be obtained through SE data fitting. The latter should be enabled by a scientifically correct model, in order to reliably extract a variety of physical properties.

For ultra-thin films, the refractive index and the thickness are likely correlated to each other in the model [28]. In other words, actual change of the physical thickness can be interpreted as a change of the refractive index; this significantly lowers the confidence on the calculated thickness values. For a multi-layer structure, fixing in the model both thickness and optical function values for the layers which are known, can significantly reduce the probability of such correlation. The SiO_2 layer thickness was measured *ex-situ* before deposition. Together with the known optical functions, all SiO_2 properties were further fixed in the optical model. The HWALD W thickness evolution was *in-situ* monitored, followed by *ex-situ* data processing for refining the extracted characteristics. Briefly, the layer of interest was first modeled using the tabulated properties available in the software [40] and then parameterized by Kramers-Kronig consistent B-spline fitting with an energy resolution of 0.1 eV, for both layer thickness and optical constants. Further parameterization using the Drude-Lorentz oscillator model was omitted because of the uncertainty in obtaining a unique solution. An example of SE data fitting with B-splines is shown in Fig. 4, indicating a good fit. The parameter uniqueness test (see the inset) reveals not a sharp minimum, which may indicate a slight parameter correlation. From MSE, the fitted film thickness has an error margin of about 4%.

Fitting the SE data for the four fabricated wafers reveals the HWALD-W-layer thicknesses of 9.6 ± 0.4, 6.3 ± 0.2, 5.2 ± 0.1 and 2.5 ± 0.1 nm. One should bear in mind that the SE measurements were performed on the 1 × 1 cm^2 area in the center of each wafer.

As expected, the growth per cycle (GPC), in the range where GPC stabilizes, is quite similar from wafer to wafer, ranging between 0.022 and 0.026 nm/cycle. A constant GPC is a characteristic of an established ALD process. Some deviations may
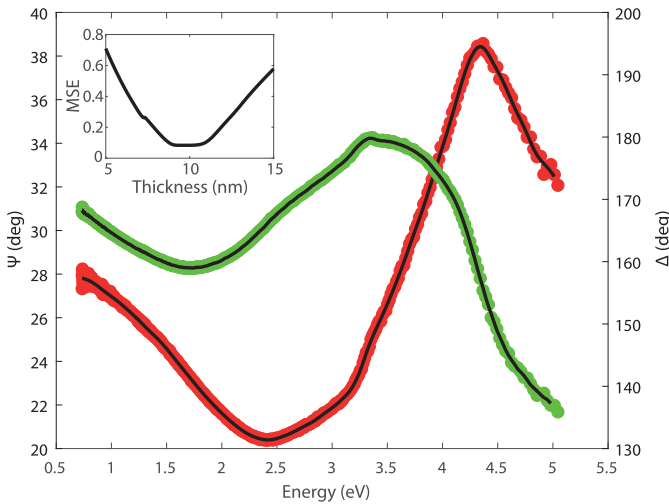
Fig. 4. Spectroscopic ellipsometry parameters Ψ (red) and Δ (green). The fit obtained by the model for both parameters is indicated by the black lines. The inset shows the parameter uniqueness of the W film thickness (MSE).
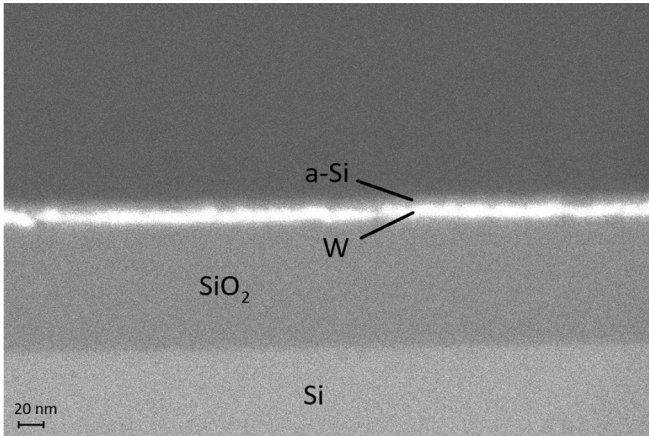

Fig. 5. High-resolution scanning electron microscopy image (obtained with an ESB detector) of the Si substrate with a roughly 100 nm thick thermal SiO₂ layer, 10 nm HWALD W film (the bright layer) and a-Si capping layer.

be expected during the initial-growth stage because of the film-nucleation conditions; the latter can vary due to, for example, slightly different seed layer thicknesses.

A necessary step towards verifying validity of the proposed SE model is measuring the thickness by alternative non-optical techniques. For this, we applied high-resolution scanning electron microscopy (HR-SEM). The images were obtained in two modes by using (i) standard in-line and (ii) energy selective backscattered (ESB) detector. A filtering grid was installed in front of the ESB detector to adjust the threshold energy for enhancing the contrast and resolution; this was especially useful in application to ultra-thin films studied in this work. Fig. 5 shows a HR-SEM image of the layer stack close to the center of the wafer. The contrast difference between the layers provides a clear visualization of the HWALD W film with a thickness estimated at 10 nm thick, consistent with the SE-model prediction (9.6 ± 0.4 nm).

V. ELECTRICAL MEASUREMENT RESULTS

A. Sheet Resistance

The sheet resistance of the W films was measured using Van der Pauw structures. Fig. 6 shows the cumulative R_{sh} plots of the differently thick W films. It can be seen that R_{sh} increases with decreasing film thickness. The black curve indicates the magnitude of R_{sh} which is expected by the bulk model, i.e., for bulk α-W resistivity (5.6 $\mu\Omega\cdot$cm, [41]). The measured R_{sh} is higher than that of bulk α-W on each of the wafers. The relative difference decreases towards thicker layers, indicating that the resistivity approaches the bulk value. The deviation of R_{sh} from the bulk value can be explained by the charge-carrier scattering effects in thin films [42], meaning reducing the carrier mobility. Scattering occurs on grain boundaries and thus increases for thinner films because of the smaller crystal grains. Additionally, the surface itself may play a role if the carrier (i.e., electron) mean free path becomes comparable with the film thickness and roughness. Finally, carrier concentration can be reduced in thin films compared to their bulks as a result of electron trapping by various defects present at both boundaries and surface.

Further, significant variations of R_{sh} are obtained across each wafer. For the thinner layers, the variations are presumably due to the small thickness non-uniformity of the W. As has been demonstrated in the earlier work [18], [43], R_{sh} of ultra-thin metallic layers can be extremely sensitive to very small thickness variations. The cumulative R_{sh} plot of the 9.6-nm HWALD W film has been divided into two series. The variations of the R_{sh} are attributed mainly to a change in W crystallinity across the wafer. The W film on the bottom half of the wafer shows significantly larger R_{sh}, compared to the top half (see the inset).

X-ray diffraction (XRD) measurements have been performed to determine the crystal-phases present in the two different wafer parts (see Fig. 7) of the 9.6-nm HWALD W film. The tungsten peaks within the measurement range are located at 40.2° [(110) plane], 58.2° [(200) plane] and 73.2° [(211) plane] for α-W [44], and at 35.5° [(002) plane], 39.8° [(012) plane] and 43.8° [(112) plane] for β-W [45], [46]. It is difficult to distinguish the peaks around ~40° due to possible overlap. However, the peaks at 35.5°, 58.2° and 73.2° suggest that the top-half of the wafer contains primarily α-W, while the bottom-half of the wafer contains primarily β-W. The two different crystal phases are assumed to originate from the asymmetrical precursor flow over the wafer and the corresponding difference in the layer crystallization process as function of the growth time [17]. The resistivity of the 10-nm-thick α-W is estimated at $\rho = 32$ $\mu\Omega \cdot$ cm, which is roughly six times larger than the bulk resistivity of α-W. The resistivity of the 10-nm-thick β-W is estimated at $\rho = 121-172$ $\mu\Omega\cdot$cm which is at the lower margin of the bulk resistivity range reported for β-W (100 − 1290 $\mu\Omega \cdot$ cm, [47]–[49]). It should however be noted that the latter was obtained for sputtered W films. In contrast to that, HWALD W films may have a reduced surface roughness (due to, for example, a much lower deposition rate), keeping the impact of roughness on resistivity minimized.
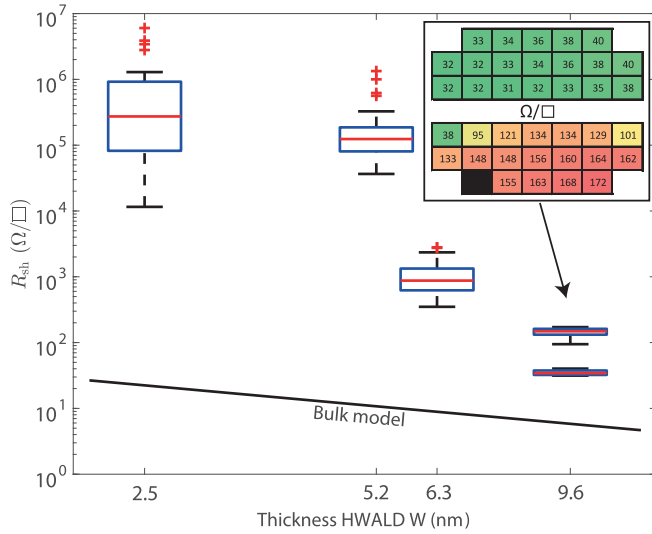
Fig. 6. The sheet-resistance variations across differently thick (as measured in the central 1×1 cm^2 area on each wafer) wafers. The middle-box line indicates the median, the lower and upper edges of each box show the data points statistically falling into the 25% to 75% range, respectively. The error bars indicate the most extreme data excluded from the 25%-75% range but still not classified as outliers. The several outliers are plotted individually using the (+) symbol. The black line indicates the theoretical sheet resistance when bulk W resistivity is assumed. The inset shows the variations (a.o. due to the phase change from α- to β-W) in the sheet resistance across the wafer for the 10 nm HWALD W wafer.
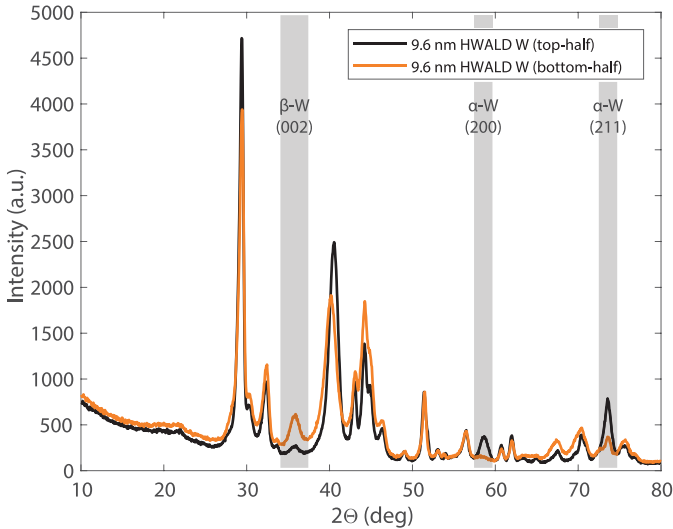

Fig. 7. 2Θ X-ray diffraction measurements of the top- and bottom-half of the 9.6 nm HWALD W wafer.

Due to the variations in HWALD W film thickness across each wafer and the difficulty to measure the film thickness outside the center of the wafer, all thin-film properties in the remaining part of this work are plotted against the sheet resistance and not the film thickness.

B. Contact Resistance and Transfer Length

To measure the contact resistance and the transfer length, the CTLM structures with 9.6-nm- and 6.3-nm-thick HWALD W layers were analysed. From Fig. 8(a), one might suggest a slight increase of the R_C with increasing R_{sh}, which can be
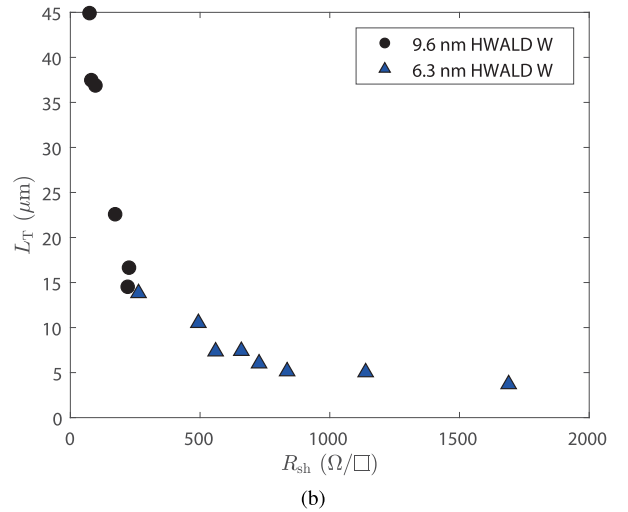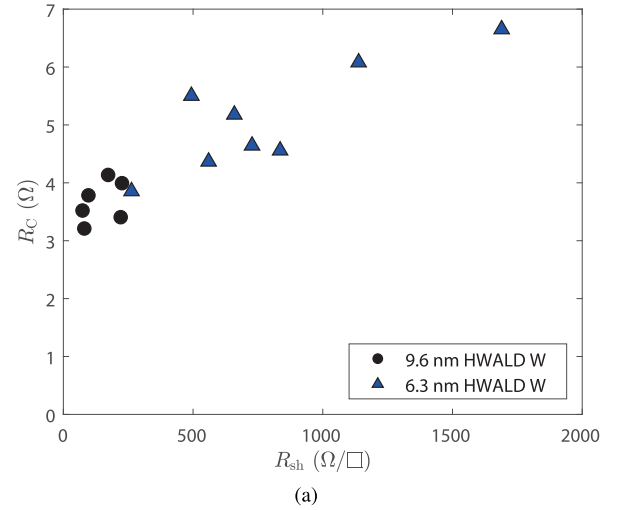

(a)

(b)

Fig. 8. The (a) contact resistance and (b) transfer length as a function of the sheet resistance. The black circles correspond to the structures with the 9.6 nm W, while the blue triangles represent the structures having the 6.3 nm film.

explained by increased current crowding and quantum confinement in the thinner layers. However, no conclusive observation can yet be drawn due to large scattering of the data points. L_T is shown to increase sharply with decreasing sheet resistance (see Fig. 8(b)). This can be explained by the relative change of the magnitude of R_{sh} with respect to the resistance of the electrodes. For higher R_{sh}, the current will be transferred between the electrode and the sheet over a shorter length near the edge of the electrode, thereby taking the least resistance path. One should bare in mind that the magnitude of L_T for small sheet resistance becomes such that $R_{el} \gg 4L_T$ does not hold anymore. In future work, R_{el} has to be chosen more conservatively.
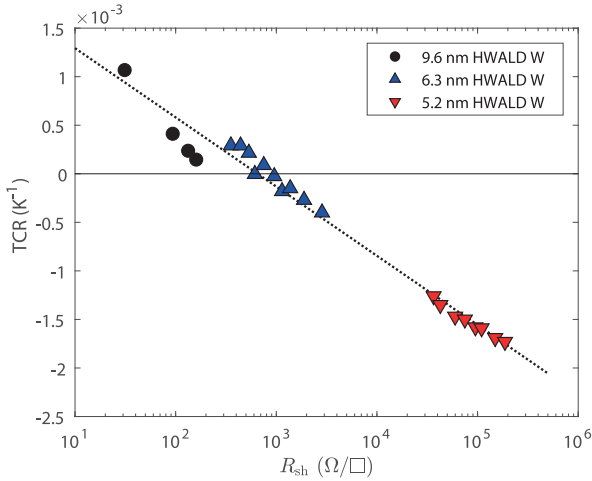
C. Temperature Coefficient of Resistance

The temperature coefficient of resistance (TCR) was obtained from the Van der Pauw structures. Standard sheet resistance measurements were performed at temperatures
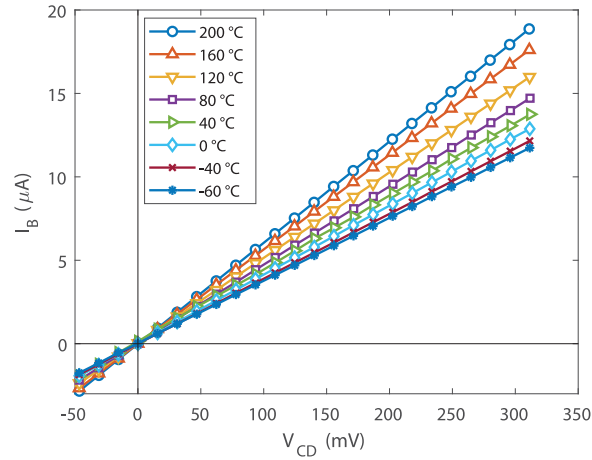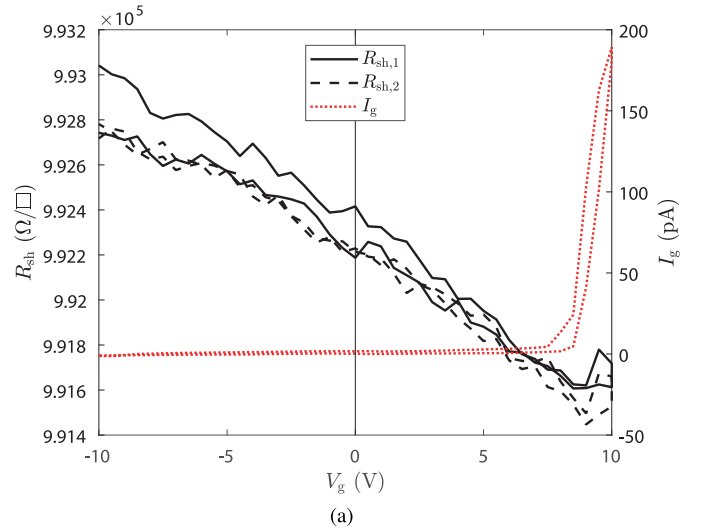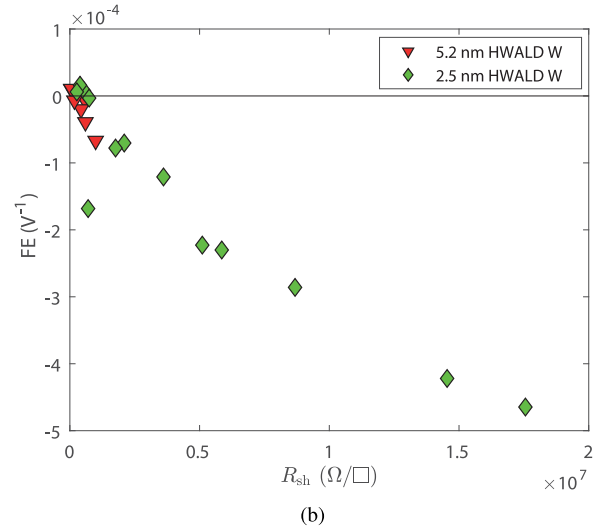
(a)
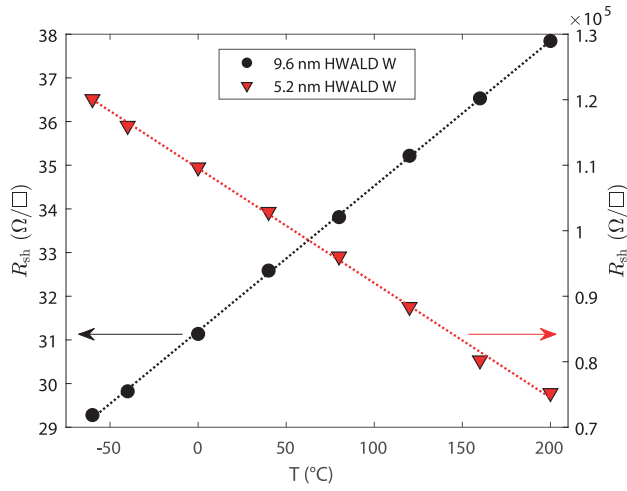
(b)

(c)

Fig. 9. Temperature dependent sheet resistance measurements. (a) IV curves of a selected 5.2-nm-thick structure. (b) Sheet resistance of selected 9.6-nm- and 5.2-nm-thick structures showing a positive and negative TCR, respectively. (c) The cumulative TCR versus sheet resistance plot for various film thicknesses (wafers) and structure positions on each wafer.

(a)

(b)

Fig. 10. (a) The change of the sheet resistance of a selected 1-nm-thick structure while sweeping the back-gate voltage V_g from -10 V to 10 V and backwards; the flat curve with a sharp increase at $\sim$8 V corresponds to the gate leakage current I_g. (b) The observed field effect as a function of the sheet resistance, for the indicated film thicknesses (wafers) and various structure positions on each wafer.

better visualize the change in R_{sh} with temperature. Fig. 9(b) shows the evolution of R_{sh} as a function of temperature for structures with differently thick W films. The magnitude of the TCR is determined by TCR = $1/R_{sh,T=0\ °C} \times (\Delta R_{sh}/\Delta T)$, where ΔR_{sh} is the change in R_{sh} due to a change in temperature ΔT and $R_{sh,T=0\ °C}$ is the R_{sh} measured at $T = 0$ °C. The TCR values change from positive to negative with decreasing the film thickness. Metals normally exhibit a positive TCR, which is explained by increased phonon scattering at elevated temperatures [50]. The observed negative TCR of the thinnest films can be attributed to for example the dominant hopping-type conductance in the percolated but still not-fully-closed W film [51]. Further, for even thinner layers, a bandgap can open and a metal can start behaving as a semimetal [43]. Fig. 9(c) gives an overview of the measured TCR for structures with various film thicknesses. It can be seen that the

ranging from -60 to +200 °C. The current-voltage $(I - V)$ measurements of a selected structure are shown in Fig. 9(a). The negative bias range is largely excluded from the plot, to

6.3 nm layer corresponds to the transition region; for this film the TCR is small and can be either positive or negative (significant variations observed across the wafer). The largest TCR of $1.1 \cdot 10^{-3}$, measured on a 9.6-nm-thick structure, is still significantly smaller than the value of the TCR for bulk W ($4.5 \cdot 10^{-3}$, [52]). It shows that thin-film effects already play a role for this thickness, though not dominantly.

D. Field Effect

The field effect (FE) measurements were conducted by applying a constant current bias (0.1 - 10 μA) between two adjacent Van der Pauw terminals, while measuring the voltage difference between the other two terminals as a function of the voltage (V_g, swept from -10 to 10 V and back) applied to the back gate. This allowed to monitor the R_{sh} modulation as a function of the back-gate electric field. Fig. 10(a) gives an example of such a $R_{sh} - V_g$ dependence, showing a little hysteresis. The FE (in V^{-1}) was defined accordingly to $FE = 1/R_{sh}(V_g = 0) \times (\Delta R_{sh}/V_g)$, where the ΔR_{sh} represents the corresponding change of R_{sh} due to the applied V_g, and $R_{sh}(V_g = 0)$ is the R_{sh} measured at zero V_g. Fig. 10(b) gives an overview of all FE measurements that were conducted. One can see that the FE increases with increasing sheet resistance. This is expected as the higher R_{sh} can be directly related to the lower electron concentration [43]. The devices with the lowest sheet resistance exhibit near zero FE. The largest field effect of $\sim 4.6 \cdot 10^{-4}$ V^{-1} is larger than the typical magnitude of the field effect in metals ($\sim 10^{-5}$ [5]–[10]), but smaller than that reported for ultra-thin TiN films [43]. However, varying definitions of the field effect complicate a fair comparison. Further, especially for metals, the field effect depends strongly on layer thickness. Dependence of the FE on temperature, varied between 40 and 160 °C, showed no conclusive trend.

VI. CONCLUSION

Thin (2.5–10 nm) tungsten films obtained by the novel HWALD technique have been characterized for the first time in terms of their electrical performance. The developed SE model, verified by HR-SEM, could adequately describe the film thickness. The XRD analysis indicated the formation of both $\alpha-$ and $\beta-$phase tungsten in the thickest film. Clear dependence of the sheet resistance, TCR and FE on the layer thickness has been demonstrated. The remarkable transition from positive to negative TCR at around 6.3 nm of the thickness has been observed. A field effect of $\sim 4.6 \cdot 10^{-4}$ V^{-1} has been measured, which is larger than the typical value obtained for metals so far.

REFERENCES

[1] O. Sneh, R. B. Clark-Phelps, A. R. Londergan, J. Winkler, and T. E. Seidel, "Thin film atomic layer deposition equipment for semiconductor processing," *Thin Solid Films*, vol. 402, nos. 1–2, pp. 248–261, 2002.

[2] A. Paranjpe, S. Gopinath, T. Omstead, and R. Bubber, "Atomic layer deposition of AlO$_x$ for thin film head gap applications," *J. Electrochem. Soc.*, vol. 148, no. 9, pp. G465–G471, 2001.

[3] T. Luoh, C.-T. Su, T.-H. Yang, K.-C. Chen, and C.-Y. Lu, "Advanced tungsten plug process for beyond nanometer technology," *Microelectron. Eng.*, vol. 85, no. 8, pp. 1739–1747, 2008.

[4] F. Papadatos *et al.*, "Low resistivity tungsten for 32 nm node MOL contacts and beyond," *Microelectron. Eng.*, vol. 92, pp. 123–125, Apr. 2012.

[5] H. L. Stadler, "Changing properties of metals by ferroelectric polarization charging," *Phys. Rev. Lett.*, vol. 14, no. 24, pp. 979–981, 1965.

[6] H. J. Juretschke, "Influence of the surface scattering of electrons on the metallic field effect in thin layers," *Surface Sci.*, vol. 5, no. 1, pp. 111–119, 1966.

[7] E. C. McIrvine, "Influence of boundary scattering on the metallic field effect," *Surface Sci.*, vol. 5, no. 2, pp. 171–178, 1966.

[8] A. Berman and H. J. Juretschke, "Origin of the electric field effect in silver," *Appl. Phys. Lett.*, vol. 18, no. 10, pp. 417–418, 1971.

[9] R. Dimmich and F. Warkusz, "A simple model of the electric field effect in thin metallic films," *Thin Solid Films*, vol. 79, no. 2, pp. 173–184, 1981.

[10] R. Dimmich and F. Warkusz, "The metallic field effect in thin polycrystalline films," *Thin Solid Films*, vol. 135, no. 1, pp. 43–50, 1986.

[11] S. M. George, "Atomic layer deposition: An overview," *Chem. Rev.*, vol. 110, no. 1, pp. 111–131, 2009.

[12] B. S. Lim, A. Rahtu, and R. G. Gordon, "Atomic layer deposition of transition metals," *Nat. Mater.*, vol. 2, no. 11, pp. 749–754, 2003.

[13] V. V. Afanas'ev, J. M. M. de Nijs, P. Balk, and A. Stesmans, "Degradiation of thermal oxide of the Si/SiO$_2$/Al system due to vacuum ultraviolet irradiation," *J. Appl. Phys.*, vol. 78, no. 11, pp. 6481–6490, 1995.

[14] A.Y. Kovalgin *et al.*, "Hot-wire Assisted ALD: A study powered by in situ spectroscopic ellipsometry," *Adv. Mater. Interfaces*, vol. 4, no. 18, 2017, Art. no. 1700058.

[15] M. Yang, A. A. I. Aarnink, A. Y. Kovalgin, R. A. M. Wolters, and J. Schmitz, "Hot-wire assisted ALD of tungsten films: *In-situ* study of the interplay between CVD, etching, and ALD modes," *Physica Status Solidi (A) Appl. Mater. Sci.*, vol. 212, no. 7, pp. 1607–1614, 2015.

[16] M. Yang, A. A. I. Aarnink, A. Y. Kovalgin, D. J. Gravesteijn, R. A. M. Wolters, and J. Schmitz, "Comparison of tungsten films grown by CVD and hot-wire assisted atomic layer deposition in a cold-wall reactor," *J. Vacuum Sci. Technol. A Vacuum Surfaces Films*, vol. 34, no. 1, 2016, Art. no. 01A129.

[17] M. Yang, A. A. I. Aarnink, R. A. M. Wolters, J. Schmitz, and A. Y. Kovalgin, "Effects of oxygen, nitrogen and fluorine on the crystallinity of tungsten by hot-wire assisted ALD," *ECS J. Solid-State Sci. Technol.*, vol. 6, no. 12, pp. P839–P844, 2017.

[18] M. Yang, A. A. I. Aarnink, J. Schmitz, and A. Y. Kovalgin, "Low-resistivity α-phase tungsten films grown by hot-wire assisted atomic layer deposition in high-aspect-ratio structures," *Thin Solid Films*, vol. 646, pp. 199–208, Jan. 2018.

[19] M. Yang, A. A. I. Aarnink, J. Schmitz, and A. Y. Kovalgin, "Inherently area-selective hot-wire assisted atomic layer deposition of tungsten films," *Thin Solid Films*, vol. 649, pp. 17–23, Mar. 2018.

[20] K. van der Zouw, A. A. I. Aarnink, J. Schmitz, and A. Y. Kovalgin, "Electrical characterization of hot-wire assisted atomic layer deposited tungsten films," in *Proc. IEEE ICMTS*, Mar. 2019, pp. 48–53.

[21] L. J. van der Pauw, "A method of measuring specific resistivity and hall effect of discs of arbitrary shape," *Philips Res. Rep.*, vol. 13, no. 1, pp. 1–9, 1958.

[22] L. J. van der Pauw, "A method of measuring the resistivity and Hall coefficient on lamellae of arbitrary shape," *Philips Techn. Rev.*, vol. 20, no. 8, pp. 220–224, 1958.

[23] W. Versnel, "Analysis of symmetrical Van der Pauw structures with finite contacts," *Solid-State Electron.*, vol. 21, no. 10, pp. 1261–1268, 1978.

[24] A. J. Willis and A. P. Botha, "Investigation of ring structures for metal–semiconductor contact resistance determination," *Thin Solid Films*, vol. 146, no. 1, pp. 15–20, 1987.

[25] J. H. Klootwijk and C. E. Timmering, "Merits and limitations of circular TLM structures for contact resistance determination for novel III-V HBTs," in *Proc. IEEE Int. Conf. Microelectron. Test Structures*, vol. 17, 2004, pp. 247–252.

[26] G. S. Marlow and M. B. Das, "The effects of contact size and non-zero metal resistance on the determination of specific contact resistance," *Solid-State Electron.*, vol. 25, no. 2, pp. 91–94, 1982.

[27] M. Ahmad and B. M. Arora, "Investigation of AuGeNi contacts using rectangular and circular transmission line model," *Solid-State Electron.*, vol. 35, no. 10, pp. 1441–1445, 1992.

[28] H. Fujiwara, *Spectroscopic Ellipsometry: Principles and Applications*. Chichester, U.K.: Wiley, 2007.

[29] H. G. Tompkins and E. A. Irene, *Handbook of Ellipsometry*. Norwich, NY, USA: William Andrew, 2005.

[30] G. E. Jellison and F. A. Modine, "Optical functions of silicon between 1.7 and 4.7 eV at elevated temperatures," *Phys. Rev. E, Stat. Phys. Plasmas Fluids Relat. Interdiscip. Top.*, vol. 27, no. 12, pp. 7466–7472, 1983.

[31] C. M. Herzinger, B. Johs, W. A. McGahan, J. A. Woollam, and W. Paulson, "Ellipsometric determination of optical constants for silicon and thermally grown silicon dioxide via a multi-sample, multi-wavelength, multi-angle investigation," *J. Appl. Phys.*, vol. 83, no. 6, pp. 3323–3336, 1998.

[32] S. Roberts, "Optical properties of Nickel and Tungsten and their interpretation according to Drude's formula," *Phys. Rev.*, vol. 114, no. 1, pp. 104–115, 1958.

[33] J. H. Weaver, C. G. Olson, and D. W. Lynch, "Optical properties of crystalline tungsten," *Phys. Rev. B, Condens. Matter*, vol. 12, no. 4, pp. 1293–1297, 1975.

[34] L. F. Mattheis, "Fermi surface in tungsten," *Phys. Rev.*, vol. 139, no. 6A, pp. 1893–1904, 1965.

[35] P. Romaniello, P. L. de Boeij, F. Carbone, and D. van der Marel, "Optical properties of BCC transition metals in the range 0–40 eV," *Phys. Rev. B, Condens. Matter*, vol. 73, no. 7, 2006, Art. no. 075115.

[36] P. Gravier, G. Chassaing, and M. Sigrist, "Optical properties of thin films of BCC transition metals," *Thin Solid Films*, vol. 57, no. 1, pp. 93–98, 1979.

[37] J. E. Nestell, Jr., R. W. Christy, M. H. Cohen, and G. C. Ruben, "Structure and optical properties of evaporated films of the Cr- and V-group metals," *J. Appl. Phys.*, vol. 51, no. 1, pp. 655–660, 1980.

[38] D. Davazoglou, G. Pallis, V. Psycharis, M. Gioti, and S. Logothetidis, "Structure and optical properties of tungsten thin films deposited by pyrolysis of W(CO)$_6$ at various temperatures," *J. Appl. Phys.*, vol. 77, no. 11, pp. 6070–6072, 1995.

[39] A. G. Deineka, A. A. Tarasenko, L. Jastrabik, D. Chvostova, and J. Bousek, "An ellipsometric study of W thin films deposited on Si," *Thin Solid Films*, vol. 339, nos. 1–2, pp. 216–219, 1999.

[40] E. D. Palik, Ed., *Handbook of Optical Constants of Solids*. San Diego, CA, USA: Academic, 1998, pp. 358–368.

[41] R. A. Serway, *Principles of Physics*, 2nd ed. Fort Worth, TX, USA: Saunders College, 1998, p. 602.

[42] G. P. Zhigal'Skii and B. K. Jones, *The Physical Properties of Thin Metal Films*. New York, NY, USA: Taylor and Francis, 2003.

[43] H. Van Bui, A. Y. Kovalgin, J. Schmitz, and R. A. M. Wolters, "Conduction and electric field effect in ultra-thin TiN films," *Appl. Phys. Lett.*, vol. 103, no. 5, 2013, Art. no. 051904.

[44] F. Allen, O. Kennard, D. Watson, L. Brammer, A. Orpen, and R. Taylor, *International Tables for Crystallography*. Dordrecht, The Netherlands: Kluwer, 1995.

[45] E. Lassner and W. D. Schubert, *Tungsten: Properties, Chemistry, Technology of the Elements, Alloys, and Chemical Compounds*. New York, NY, USA: Kluwer, 1999.

[46] A. Bartl, "Fundamentals of NS-tungsten powder manufacture," Ph.D. dissertation, Inst. Chem. Technol. Inorganic Materials, Tu Vienna, Vienna, Austria, 1997.

[47] P. M. Petroff, T. T. Sheng, A. K. Sinha, G. A. Rozgonyi, and F. B. Alexander, "Microstructure, growth, resistivity, and stresses in thin tungsten films deposited by RF sputtering," *J. Appl. Phys.*, vol. 44, no. 6, p. 2545, 1973.

[48] Q. Hao, W. Chen, and G. Xiao, "Beta (β) tungsten thin films: Structure, electron transport, and giant spin Hall effect," *Appl. Phys. Lett.*, vol. 106, no. 8, 2015, Art. no. 182403.

[49] P. M. Petroff and W. A. Reed, "Resistivity behavior and phase transformations in β-W thin films," *Thin Solid Films*, vol. 21, no. 1, pp. 73–81, 1974.

[50] N. W. Ashcroft and N. D. Mermin, *Solid-State Physics*. New York, NY, USA: Harcourt Brace College, 1976.

[51] H. Bottger and V. V. Bryksin, "Hopping conductivity in ordered and disordered solids (I)," *Physica Status Solidi B*, vol. 78, no. 9, pp. 9–56, 1976.

[52] R. A. Serway and J. W. Jewett, *Principles of Physics: A Calculus-Based Text*, 5th ed. Belmont, CA, USA: Brooks/Cole, 2013.